Numerical analysis of mechanical behaviour of lattice and porous structures

Miguel Marco[1], Ricardo Belda[2], María Henar Miguélez[1], Eugenio Giner[2]*

[(1)] Department of Mechanical Engineering. Universidad Carlos III de Madrid. Avda. de la Universidad 30, 28911 Leganés, Madrid, Spain

[(2)] Centre of Research in Mechanical Engineering – CIIM, Department of Mechanical and Materials Engineering, Universitat Politècnica de València Camino de Vera, 46022 Valencia, Spain

**Corresponding author: Miguel Marco,* mimarcoe@ing.uc3m.es

Abstract

Lattice and porous structures have attracted attention in scientific literature due to the development of 3D printers that facilitate their manufacturing. A thorough understanding of the mechanical behaviour of these structures is necessary. In this work, several lattice and porous structures are analysed using the finite element method. Eleven configurations have been studied using periodic boundary conditions, in order to numerically estimate their elastic mechanical properties (Young's modulus, shear modulus and Poisson's ratio) as a function of the structure porosity. In addition, a tensile fracture test has been modelled to analyse the predicted fracture pattern as well as the stress-strain curve for each structure. It is shown that structures based on spherical holes distributions yield the best behaviour both in tensile and shear conditions. The distribution of cavities has a strong influence on the mechanical behaviour. The square distribution improves stiffness, while the hexagonal distribution improves the shear modulus. Random distributions clearly decrease the stiffness and strength of the structure, although the damage in these structures is more progressive. Therefore, this work provides a comparative study to assess the influence of the lattice topological structure on some mechanical properties of interest in structural engineering, as a function of porosity.

Keywords: lattice structures; topological optimization; homogenization; mechanical properties; finite element modelling

1. Introduction

The development of additive manufacturing has motivated investigations about the potential of lattice and porous structures developed for lightweight applications, such as aerospace, automotive or biomechanical engineering. Usually, lattice structures can be classified as periodic or random (stochastic) depending on their layout patterns [1]. Porous media or cellular structures are widely analysed in literature, based on bio mimicry, current designs imitate natural structures such as trabecular bone, corals, sponges, cork, etc, due to their enhanced mechanical characteristics, directly related to morphometry. For example, some lattice structures, e.g. the octet-truss lattice, have demonstrated to gain efficient stiffness-to-weight and strength-to-weight benefits because of its stretching-dominated behaviour [2] while porous materials are lightweight and have high impact absorption [3].

Traditionally, open-cell porous materials have been manufactured through liquid state processing (direct foaming, spray foaming, etc.), solid state processing (powder metallurgy, sintering of powder and fibres, etc.) or electro-deposition and vapour deposition [4,5]. Additive manufacturing technologies allow the generation of porous, reticular and lattice structures with predefined external shape and internal architecture [6], being geometries otherwise very difficult to fabricate through other manufacturing processes.

A wide collection of lattice and porous structures has been studied in the literature in order to analyse their mechanical behaviour under different loading conditions. The estimation of mechanical properties has been carried out using numerical models (see for instance [7]) or experimental tests usually performed, see for instance [8,9]. Moreover, the influence of the lattice structure design on the mechanical properties have been analysed in several works in literature [10–15]. Different aspects have been analysed, such as the influence of load orientation [15] or the consideration of anisotropic models that account for the fabrication direction [16]. Lattice structures are appropriate for a wide variety of applications, e.g. as vibration isolation [10] or energy absorption in blast-loading test [17]. The study of porous structures has also motivated several investigations [18–22]. The first approaches provided deformation mechanisms and analytical expressions of mechanical properties as a function of morphological relationships [18,19]. More recently, fatigue and failure properties have been assessed [20,21] and detailed models based on images have highlighted the major importance of morphometry on the mechanical performance of these structures [22]. Advance materials, such as composite metal foams (CMF) are formed with metal hollow spheres and a solid matrix of another. These light structures exhibit good energy absorption and are used in armour components, aircraft and automotive applications, sound absorption or filters [23]. Foam structures are easier to manufacture than lattice structures, as they can be made from bulk material with gas injection or blowing agents [5]. Numerically, foams can be modelled as random distributions or using Laguerre-Voronoi tessellations [24].

Topology optimization is an important strategy to optimize morphology or gradient density [25] through the improvement of the structural response. Its combination with additive manufacturing allows the fabrication of proper structures for specific applications, adapting the geometry to the boundary conditions and the optimization cost function of the problem. Topology optimization techniques are based on homogenization method [26], Solid Isotropic Material with Penalization (SIMP) [27], using the level set method [28] or evolutionary structural optimization (ESO) [29,30]. The ESO technique consists in the deletion of inefficient (or underloaded) parts from a structure so that the resulting topology evolves towards an optimum architecture [29,30]. The evolution of the ESO method is named as the bidirectional ESO (BESO), which not only removes low efficient parts, but also reinforces the parts where needed to improve its objective function [31]. The BESO technique was improved to overcome non-convergence and mesh dependency problems of the original version [32]. After that, it has been demonstrated that the new BESO method is able to help in the topology optimization for macro-structures with high computational efficiency [7].

Due to the increasing applications of lattice and porous structures, it is important to characterise their behaviour under different loading configurations (tension/compression and shear). A numerical homogenization procedure can provide the mechanical constants required as an input in further finite element (FE) models at a larger scale. In this work, some designs of lattice structures proposed in the literature and other architectures obtained through topological optimization are analysed, including mechanical characterization and fracture propagation modelling. The influence of porosity on the elastic constants of each morphology is also explored. Structures analysed in this work could be useful in fields where the structure needs to support the required loading conditions, while it keeps its lightness and porosity. We consider that this study can be useful for fields of research such as bone implants or replacement, prosthesis or aerospace applications.

This article is organized as follows. Section 2 reviews the lattice and porous structures considered in this work. Some of them have been designed using topological optimization, as detailed in Section 3. The procedure followed for the finite element modelling is explained in Section 4. Section 5 presents the results and discussions, including a validation versus some experimental tests, an analysis of the influence of the element type, the estimation of the mechanical constants and the results obtained in the simulated fracture tests. The main conclusions of this work are summarized in Section 6.

2. Architecture of the structures

A wide variety of structure designs can be found in the literature, see for instance the architectures proposed in [33,34]. In this work, the most used configurations are selected for study. Each structure is based on an elemental 3D cubic cell, repeated in the three directions of space to use a periodic boundary conditions (PBCs) approach to calculate the corresponding elastic constants associated to each morphology. In order to dispose of models of porosities between 10% and 90%, the characteristic parameters of each architecture are varied. Each lattice structure is shown in Fig. 1 with a porosity about 70%. Henceforth, names in brackets and capital letters will be used to denote each structure.

1. Cubic cellular unit (CCU). Consists of bars in each edge of the cube.
2. Diagonal cubic cellular unit (CCU-DIAG). Including bars in the diagonals and edges of the cube.
3. Diagonal (DIAG). With bars only in the diagonal axes of the cube.
4. Spheres with square distribution (SPH-SQ). A porous structure developed with spherical voids, following a square distribution.
5. Spheres with hexagonal distribution (SPH-HEX). Porous structure formed with spherical voids, following a hexagonal distribution.
6. Spheres with random distribution (SPH-RND). Porous structures formed with a random distribution of spherical voids. Intersection of the voids is allowed to obtain models of high porosities.

7. Octet truss (OCT). A common design used in lattice structures, composed by an octahedral cell surrounded by eight tetrahedral cells [2,14].
8. Kelvin cell (KEL-CELL). Also called tetrakaidekahedron, has spherical geometry, with fourteen faces, eight hexagonal and six quadrilateral. This structure has been used in some works as an optimal reconstruction model of real foam structures [24].
9. Random truss (TRUSS-RND). Based on the idea of the Laguerre-Voronoi tessellation [24]. A random structure formed by a random point distribution, where the neighbouring points are connected by bars. It is similar to trabecular bone distribution, where each trabecula is a bar.
10. BESO optimization, maximizing E in tension test (OPT-E-TENS). Structure designed using the BESO technique, seeking for the maximum Young's modulus (E) under traction boundary conditions.
11. BESO optimization, maximizing G in shear test (OPT-G). Structure designed using the BESO technique, seeking for the maximum shear modulus (G).

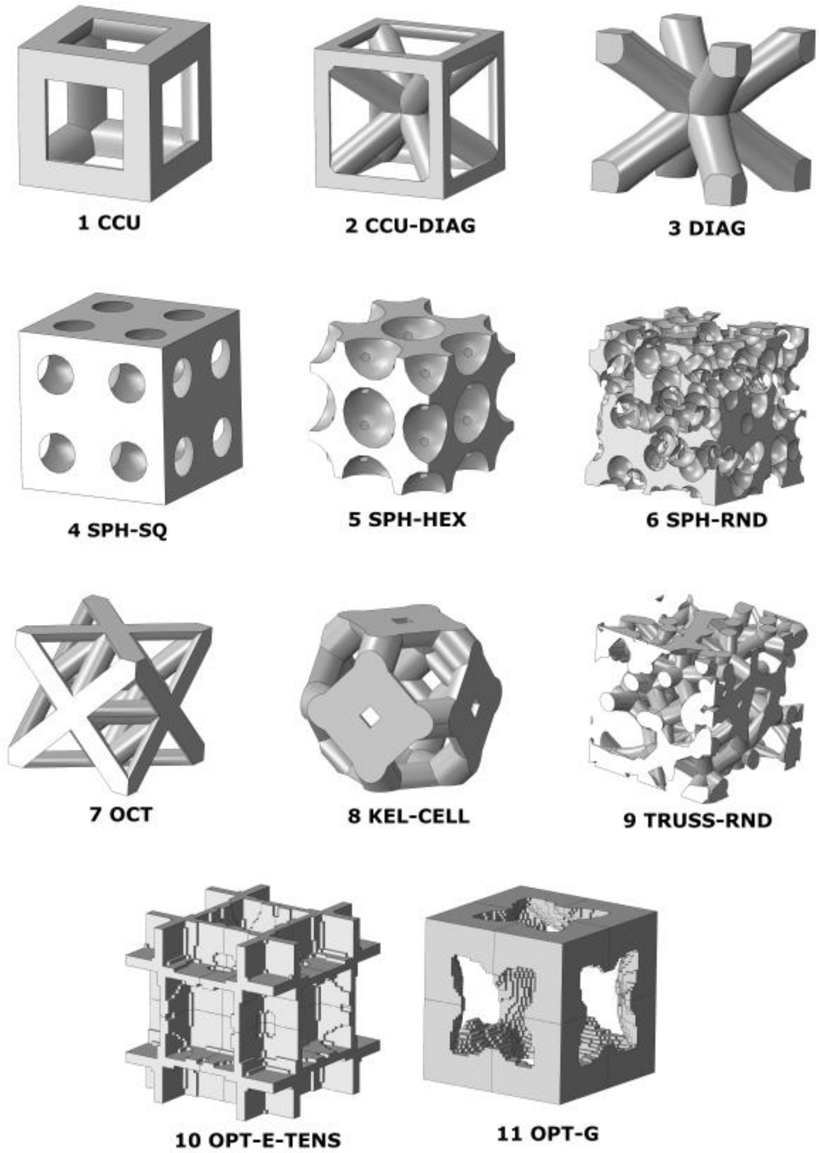

Figure 1. Lattice and porous structures analysed in this work. The structures depicted in this figure have a porosity of about 70%.

Each structure has been analysed for a range of porosity from 10% to 90%. As an example, cases shown in Fig. 1 present a porosity of about 70% that enables the visualization of the internal and external morphology of the cell.

3. Bidirectional evolutionary structural optimization (BESO)

Through an optimization process, functional structure designs can be created to optimize mechanical parameters. The BESO technique is used to create reticular structures adapted to the different boundary conditions studied in this work (see Fig. 1, structures 10 and 11). Although several optimization techniques exist, we use the BESO technique, which is developed from the Evolutionary Structural Optimization (ESO) method [29,30]. The original ESO technique is a heuristic method based on removing inefficient zones from a structure. ESO technique has been improved in last years, leading to the new version called the bidirectional ESO (BESO), which not only removes elements from the least efficient regions, but also adds elements to the most loaded regions simultaneously [31]. First versions of BESO presented some weaknesses that limited its application to the field of microstructure design [32]. A few years later, Huang, Randman and XIE [7,32] developed an improved BESO method and successfully overcome these weaknesses. In this work we use the version proposed by Zuo and Xie [35], also used in recent works [36], specifically based on finite element analysis, which treats the relative densities of elements as the design variables. For a predefined volume fraction of the design, a design variable (density) takes the value of either 1.0 indicating the presence of the element or a small number close to 0.0 indicating the deletion of the element.

Through this method, a representative volume element (RVE) of the structure has been designed to optimize a mechanical parameter, in our case, the axial and shear stiffnesses. It consists of an iterative process, and in this work it has been implemented with a Python script to interact with the software Abaqus/CAE. In our topology optimization models, Young's modulus of solid material corresponds to E_s=1 (units of stress) and void material to $E_v=1\cdot10^{-9}$ (units of stress). Poisson's ratio is kept constant as v=0.3 for both materials.

An initial meshed cube is necessary for the first step of the BESO iteration technique. The model needs a small variation in the geometry in order to induce stresses at the first iteration in the RVE. This variation is applied to the model with the deletion of some elements (marked in red in Fig. 2). After this first step, the BESO procedure optimizes the material disposition, seeking for the maximum value of the property defined as objective. In this work, we propose 4 different initial steps (instead of the only one proposed in [7]): v1: remove the first element from the centre of the RVE; v2:from the corners of the RVE; v3: from the centre of the faces on the RVE and v4: close to the corners but inside of the RVE. The scheme of the first elements removed from the initial model is illustrated in Fig. 2. The corresponding boundary conditions for each case (*E* and *G* optimization) are imposed to the model at every iteration.

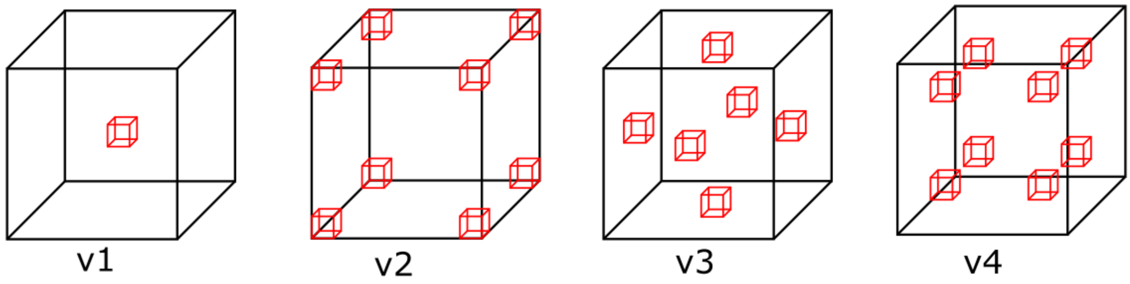

Figure 2. Four different initial states used in this work for BESO optimization. The red cubes are elements removed from the initial mesh at each design.

These design procedures (v1-v4) have been used to develop the optimization process for a porosity equal to 50%, and then, mechanical properties of each design have been calculated. Finally, only one design for each mechanical property objective has been selected, according to the best mechanical performance results, for our study. It is important to remark that in this work we are looking for the highest stiffness and ultimate stress, considering it as a good mechanical behaviour. However, in other fields of research, different goals can be necessaries for the researchers.

4. Finite element modelling

4.1. Geometry and mesh

Regarding designs obtained from the literature, the geometries have been replicated using scripts in Python with the CAD module from Abaqus, obtaining porosities ranging from 0.1 to 0.9. The structures consist of bars and spheres merged to build the final configuration. A RVE of each design studied in this work is shown in Fig. 1. These structures replicated from other works in the literature (from 1 to 9 in Fig. 1) have been modelled using tetrahedral elements with quadratic interpolation (C3D10 element type code in Abaqus) due to their good performance, good accuracy, and adaptability to the complex geometries studied in this work. For instance, random distribution structures imply complex vertexes and small edges requiring a high quality mesh. The element size has been estimated performing a mesh sensitivity analysis, leading to models that are composed of about $2{\cdot}10^5$ elements. Further refinement led to negligible effects on the results covered in the analysis.

The geometry optimized for the axial and shear stiffnesses has been obtained using the BESO technique. The final mesh connectivity and nodal coordinates of the structure are generated after an iterative process. These models have been meshed using hexahedral elements with linear interpolation (C3D8R element type code in Abaqus). Hexahedral elements are often used in topological design to simplify the process [7,13,32,35,37,38]. The element size has been set to $RVE_{size}/50$, similar to that used in other optimization works [7]. These dimensions lead to a mesh composed of a maximum of $1{\cdot}10^6$ elements, although this value decreases as porosity increases. For instance, structures with a porosity equal to 0.9 are formed by about $1{\cdot}10^5$ elements. In this work, every mesh must satisfy symmetry conditions with respect to the three planes to apply PBCs.

4.2. Boundary conditions and elastic properties estimation

The homogenization approach is used to estimate the elastic constants of repetitive structures, such as composite materials or biological tissues. It consists of the calculation of the stiffness matrix of the model, that relates a stress vector ($\sigma = (\sigma_{xx}\ \sigma_{yy}\ \sigma_{zz}\ \tau_{yz}\ \tau_{zx}\ \tau_{xy})^T$) and a strain vector ($\varepsilon = (\varepsilon_{xx}\ \varepsilon_{yy}\ \varepsilon_{zz}\ \gamma_{yz}\ \gamma_{zx}\ \gamma_{xy})^T$) through the Lamé-Hooke constitutive equation, Eq. 1

$$\sigma = C\,\varepsilon \qquad [1]$$

The homogeneous response calculation is accomplished through the combination of the PBCs and six independent unitary strain fields, three axial and three shear strains, shown in Fig. 3. Through each unitary strain field applied on each structure, the corresponding column *i* of the stiffness matrix $C_{:,i}$ is calculated. Each column of the stiffness matrix corresponds to the equilibrium stress vector σ^i, corresponding to the strain field ε^i. Stress vectors are obtained from the nodes allocated in the faces of the FE model. PBCs are considered in combination with a unit cell of large enough dimensions in order to model a representative mechanical response of the whole structure [39]. According to Reisinger *et* al. [40] when PBCs are applied to a cell, the volume of analysis must fulfil two conditions: the stress field must be periodic in such a way that the unit cell is in static equilibrium and the deformed shape of opposite sides of the unit cell must be consistent. To satisfy the second condition, the geometry and mesh of the numerical model must be symmetrical. In this work, this symmetry has been guaranteed by mirroring the principal cell with respect to the planes XY, XZ and YZ.

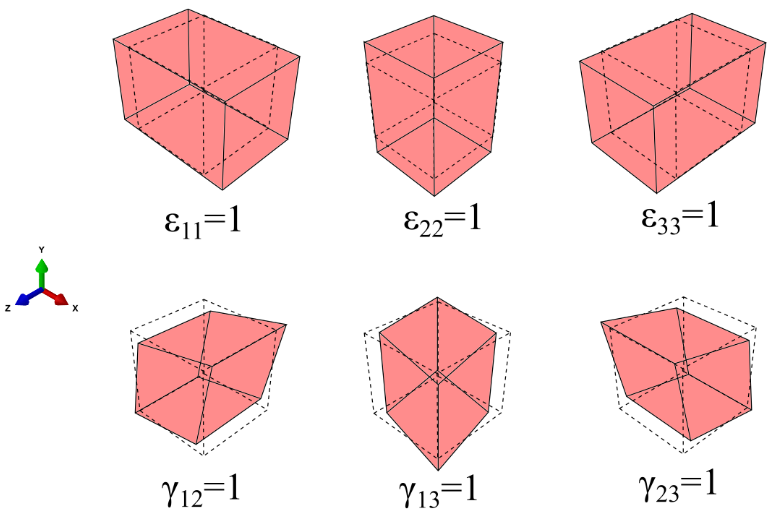

Figure 3. Scheme of the six unitary strain fields, three pure axial (top) and three pure shear (bottom) to calculate homogenized stiffness matrix in combination to PBCs of the structures analysed. Initial cell is represented with dotted lines. The deformed shapes are not shown at true scale.

In this work, constraint equations proposed in [41] to fulfil the PBCs conditions are imposed to the model by means of multi point constrains (MPCs) in Abaqus. In order to apply the MPCs in opposite nodes adequately, constrains equations must be carefully implemented in the model, using the same order of nodes in each set [42]. Using these constraint equations, the model reproduces the deformed shape corresponding to each unitary strain case, relating displacements between faces, edges and corners.

The entire process of calculation of the stiffness matrix involves several stages: create a symmetric mesh from the RVE with respect to the three reference planes, create node sets to apply PBCs to the model, imposing six independent unitary strain fields and estimating the corresponding stresses from the node sets to calculate each column of the stiffness matrix. Once the stiffness matrix has been estimated, elastic constants are calculated from the flexibility matrix $[S]$, which is obtained through the relationship $[S] = [C]^{-1}$. An orthotropic behaviour is obtained though this methodology, which is a valid assumption for the geometries under study. All the structures analysed present symmetry with respect to the three main directions, except from the random structures (SPH-RDN and TRUSS-RDN). Then, an orthotropic behaviour is expected for the symmetric structures, characterized by an axial stiffness (E), a shear stiffness (G) and a Poisson's ratio (ν). In case of the random distribution structures, we have averaged the stiffnesses along the three main directions and planes in order to compare the results with the rest of the models. The whole process has been automatized though several scripts combining Python and MATLAB and it is sketched in Fig. 4.

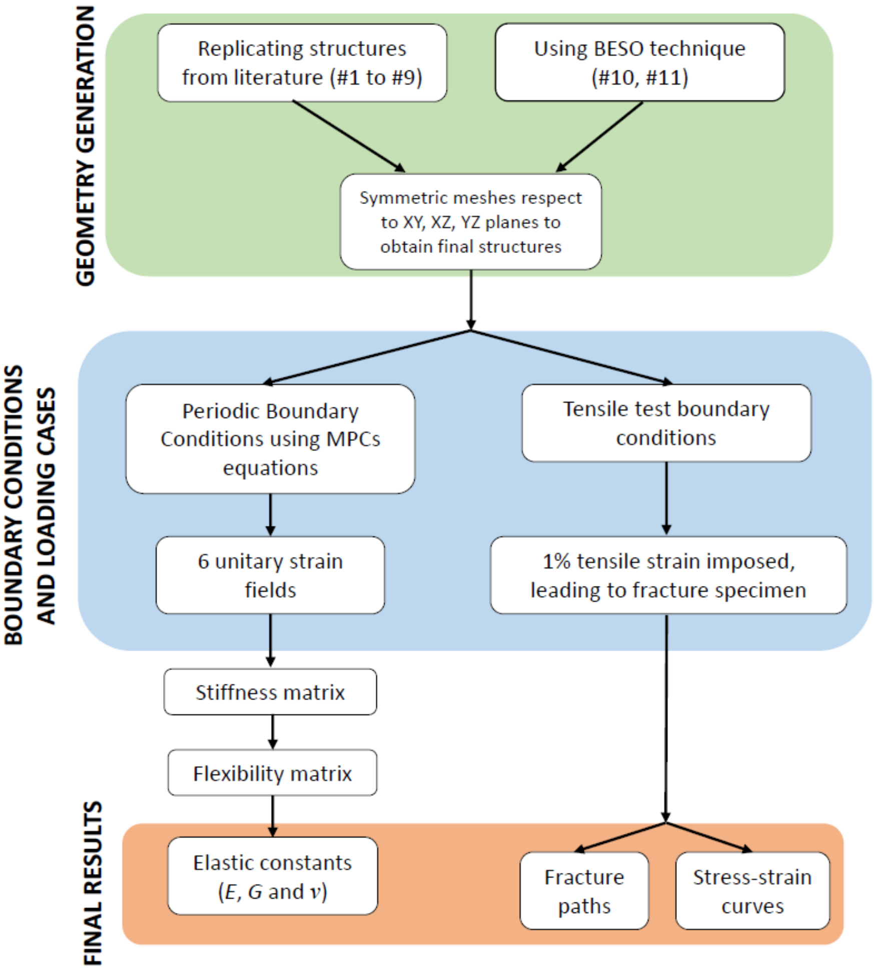

Figure 4. Scheme of the main tasks developed for this work.

4.3. <u>Tensile fracture simulation</u>

Tensile fracture has been numerically simulated for each structure, considering only designs with a porosity equal to 0.5. A displacement is imposed at nodes on the top face of the model in Z direction. On the opposite face, Z displacement is prescribed to zero. In addition, displacements at the central node at bottom face are fully constrained, to avoid solid rigid displacements of the model.

The method to simulate the fracture propagation has been also used by the authors in other works with complex geometries obtaining good results and fracture paths [43–46]. The technique is based on the degradation of elastic properties of elements that exceed a critical value in tension. The method is implemented by means of a USDFLD Abaqus subroutine. As a failure criterion, it is checked when the maximum principal stress at an element exceeds a limit value. Then, the Young's modulus of that element is reduced to a minimum value in order to simulate the loss of stiffness due to the crack.

In this section, the initial mechanical properties of the material are considered as: $E_{initial}$=1 (units of stress) and ν=0.3. We assume that failure occurs at a critical stress as $\sigma_{crit}=E/10^2$. This value was stablished taking into account relations between mechanical properties (Young's modulus and critical stress) in materials such as aluminium or Ti6Al4V. Once σ_{crit} is reached in an element, its Young's modulus is reduced to $E=E_{initial}/10^5$, a value low enough to simulate the smeared crack process. The dimensions of the model are 1×1×1 (units of volume) and a displacement equal to 0.01 (units of length) is imposed to the top face, which implies a maximum nominal strain of 1%.

5. Results and discussion

5.1. Topology optimization

As explained above, the optimization process requires an initial stress state in the cell prior to initiate the procedure. This initial stress state has been induced removing one element from the model. In this work, four different initial states (v1 to v4, illustrated in Fig. 2) have been evaluated for each optimized design. After evaluating the mechanical properties of a unit cell with a 50% porosity, one initial state (v2) was chosen for each optimization design, because it led to the highest elastic axial and shear stiffnesses (*E* and *G*). Small differences were found in final optimized structures, about 5% in *E* values and 1% in *G* values, using the different initial states explained above.

Once the initial state design was fixed, the topological optimization was carried out for a range of porosity from 10% to 90%. Fig. 5 shows the geometries obtained for each mechanical property fixed as objective (*E* and *G*) and different porosity levels (30%, 60% and 90%).

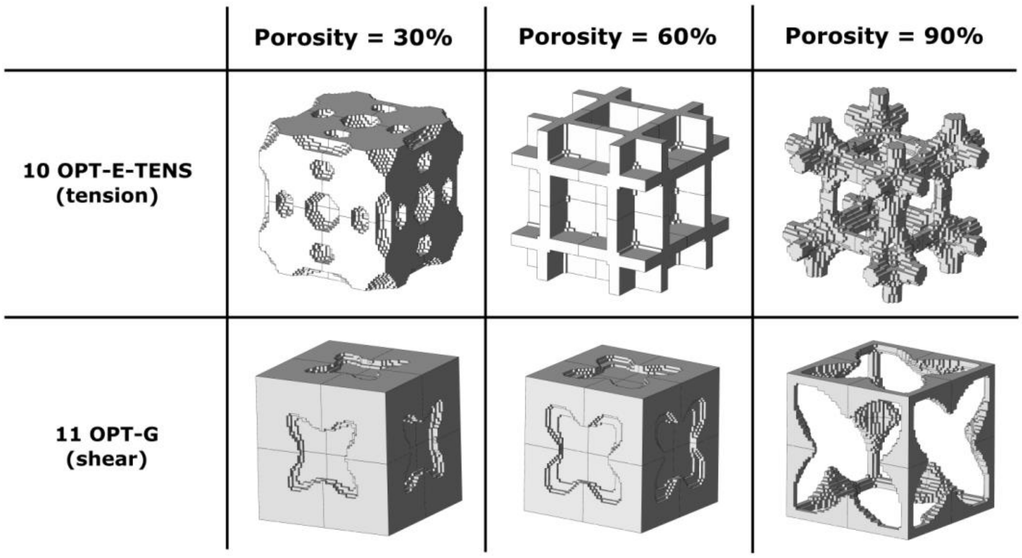

Figure 5. Optimized structures calculated in this work with porosities around 30%, 60% and 90%. Structures are optimized to obtain the maximum Young's modulus under tensile load (top) and shear modulus (bottom).

5.2. Validation and sensitivity analysis

Validation

The validation of the numerical procedure used in this work is performed through a comparison to experimental results obtained from the literature. Young's modulus obtained for DIAG structure was obtained from experiments by McKown et al. [17] under compression loading for different levels of porosity. The relationship between the relative density (in our work: $porosity = 1 - \rho_{rel}$) and the relative Young's modulus (E/E_s) of the structure was inferred from the experiments. In this work, E_s is the Young's modulus of the solid material implemented in the numerical model. McKown et al. obtained a good correlation by fitting the expression $E_{rel} = 0.95\rho_{rel}^{2.84}$, where ρ_{rel} is the relative density and E_{rel} denotes the relative elastic modulus. This expression is compared in Fig. 6 with the results of the DIAG model developed in the present work, under compression loading conditions, thus simulating the experimental tests developed by McKown et al. in [17].

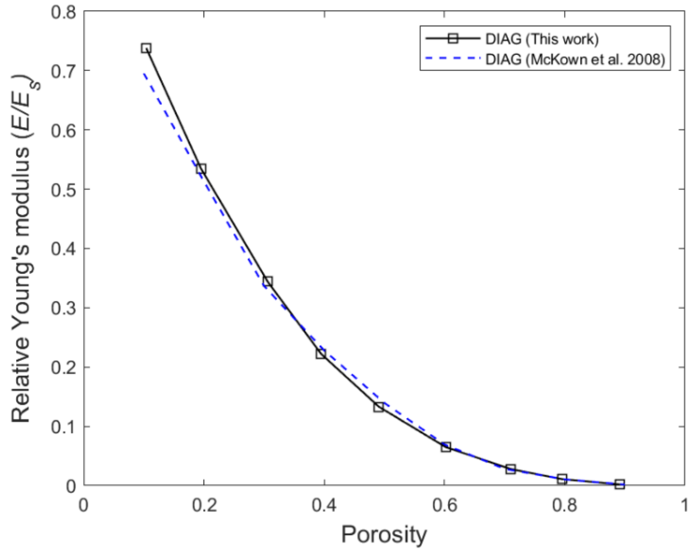

Figure 6. Validation study developed in this work for DIAG structure. Relative Young's modulus comparison for different porosities under compression conditions: numerical models developed in this work and experimental compression tests from [17].

Fig. 6 shows the ability of the numerical model to accurately reproduce the stiffness behaviour of the structure for different porosity levels, leading to an average error about 4%.

Influence of the element type

Different element types have been used in this work: tetrahedral and hexahedral elements. Designs inspired in previous works in the literature have been developed using tetrahedral elements, as explained in previous sections. The complexity of the structures requires the use of these elements, especially when random distributions are modelled. In the other hand, designs optimized through BESO technique are modelled using hexahedral elements, as hexahedral elements allow an easier modification of the topology and the boundary than with tetrahedral elements. The sensitivity of the numerical prediction of mechanical properties (*E*, *G* and *ν*) with element type was developed comparing tetrahedral and hexahedral performance during the simulation of the same structure.

CCU and SPH-SQ structures have been re-meshed with regular hexahedral elements, as those we used in the topological optimization. In Fig. 7a an internal detail of the CCU design is shown with different elements types.

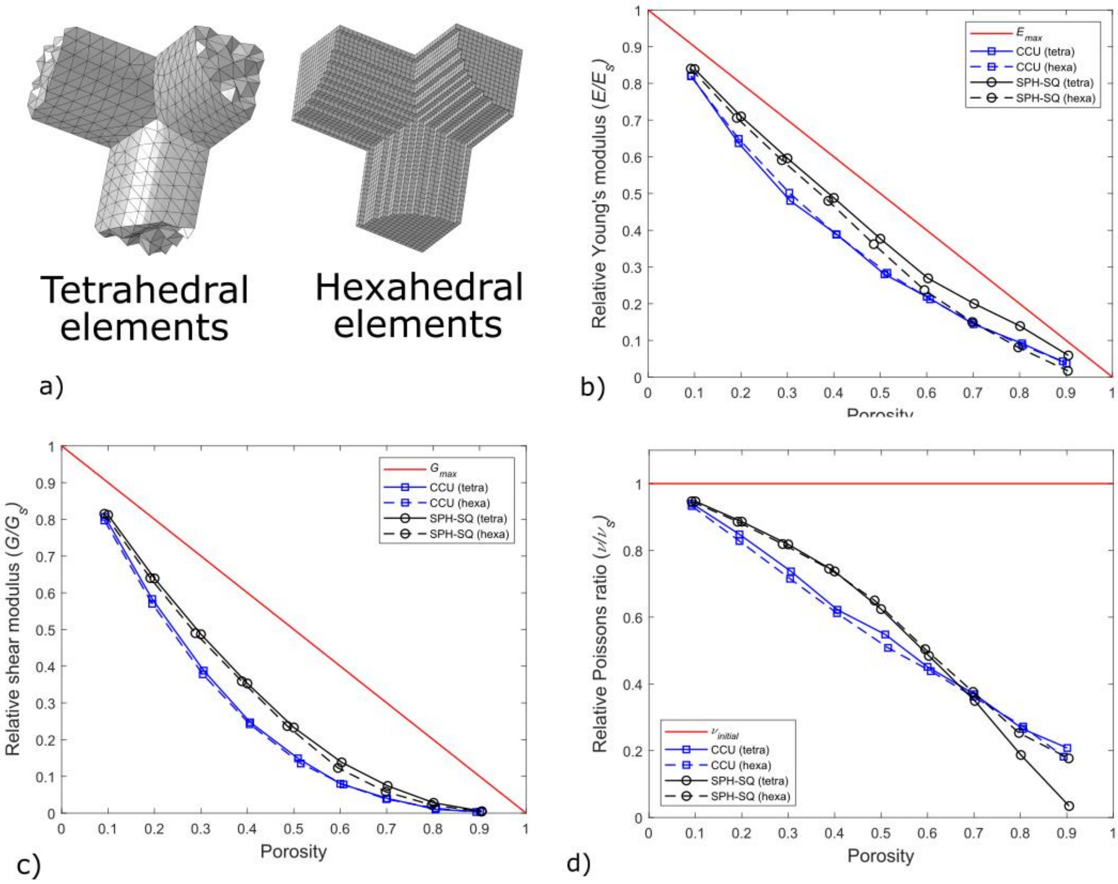

Figure 7. Influence of the element type on the mechanical constants calculated for CCU and SPH-SQ designs. a) Detail of CCU design modelled with tetrahedral elements (left) and regular hexahedral elements (right); b) relative Young' modulus for both structures and elements types; c) relative shear modulus for both structures and elements types; d) relative Poisson's ratio for both structures and elements types.

Figs 7b, 7c and 7d show the results of the element type sensitivity analysis obtained in the elastic constants: Young's modulus, shear modulus and Poisson's ratio, respectively. Little differences were found between the tetrahedral and regular hexahedral meshes, even though regular hexahedral elements do not fully fill the volume. SPH-SQ shows higher differences between meshes for porosities from 0.7 to 0.9 when Young's modulus or Poisson's ratio are estimated (see Fig 7b and 7d). In general, slight differences in the predicted mechanical behaviour of the structure are observed when the use of tetrahedral or regular hexahedral elements is compared. As explained in previous sections, a mesh sensitivity analysis was developed previously to set a proper element size, ensuring negligible influence of its size. This element size is also appropriate to avoid the influence of element type.

5.3. Elastic properties (E, G, v) estimation through homogenization

In this section, the relative mechanical properties E/E_s, G/G_s, v/v_s are estimated from the PBC models. These results have also been included in Appendix A. Fig. 8 shows an example of tensile and shear loading cases from the numerical model for the OCT design. The values of the mechanical properties have been averaged, taking into account the different values obtained in each direction or plane. In the case of random structures (SPH-RND and TRUSS-RND), five different distributions have been developed and the mean result is considered for the study. Results for E, G and v are shown in Figs. 9 and 10, respectively, plotted as normalized variables (E/E_s, G/G_s, v/v_s).

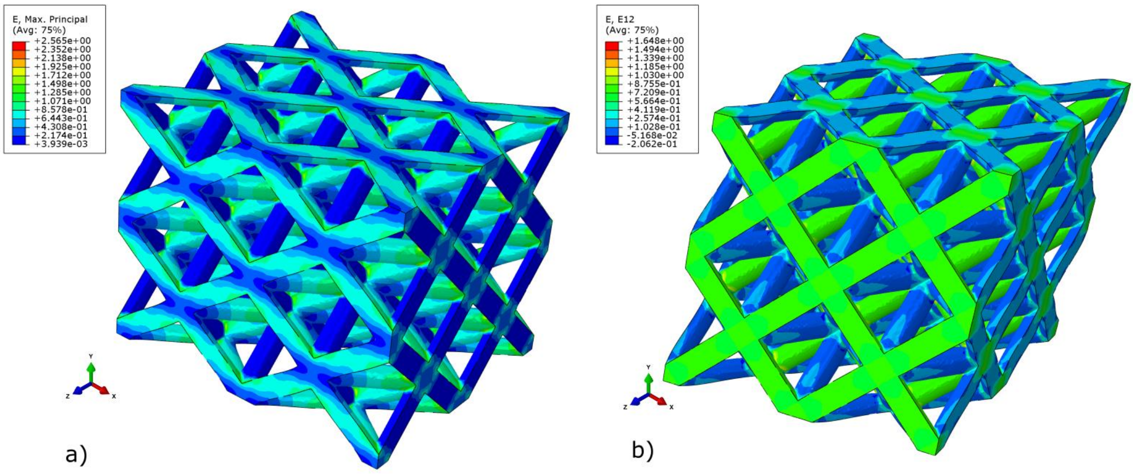

Figure 8. Numerical model of the OCT design with a porosity of around 70%. Strain contour plots under different loading conditions: a) ε_{11}=1 and b) γ_{12}=1.

Young's modulus E/E_s

Fig. 9a shows results obtained in the analysis for the relative Young's modulus for porosities ranging from 10% to 90%. A non-linear dependence on porosity is observed for most of the structures. The structures containing spherical voids with squared or hexagonal distributions (SPH-SQ and SPH-HEX) and both optimized structures (OPT-E-TENS and OPT-G) show the highest values of relative Young's modulus. As expected, random distribution designs (SPH-RND and TRUSS-RND) show poorer results. The random distribution involves the existence of thinned zones in the structure with the consequent decrease of stiffness. For example, in SPH-RND, the randomness causes strong E/E_s variations for some levels of porosity, resulting in stiffness values close to the maximum values reached by other designs. Therefore, a random distribution of material makes difficult to predict the stiffness accurately, but a range of values expected may be provided. In the results presented in Fig. 9a, it can be observed that the squared distribution (SPH-SQ) have the best performance and is the upper bound regarding axial stiffness with respect to the random spheres distribution (SPH-RDN).

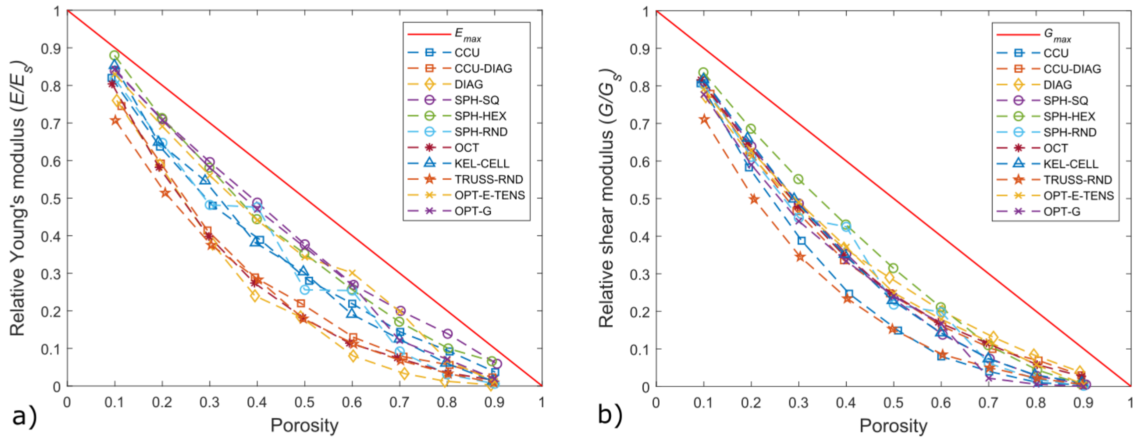

Figure 9. Results obtained for relative Young's modulus (a) and relative shear modulus (b) for different porosities.

CCU and KEL-CELL structures present analogous E/E_s behaviour which can be explained because of the similarities in the material distribution at the RVE edges, see Fig 9a. This conditions the wall deformation mechanisms and thus the elastic properties. On the other hand, CCU-DIAD, DIAG and OCT morphologies lead to the lowest E/E_s results, in the lower bound of the structures analysed, see Fig. 9a. Again, these similarities are result from the geometrical characteristics, presenting material at the diagonals of the RVE.

Results obtained by means of BESO technique are compared with the analysis developed by Huang et al. [7] where bulk and shear modulus maximum were sought, using a previous version of this technique. Considering the OPT-E-TENS design, Huang et al. [7] presented results for porosity equal to 0.5, 0.6 and 0.7. Results of models of porosity equal to 0.5 are similar to those obtained in this work, but lower porosities led to higher values of axial stiffness results in this work, about twice those presented by Huang et al. [7]. Structures calculated by Huang et al. are similar to those obtained in this work (see Fig. 5), although there are small differences on the morphometry obtained. This can be due to the use of different initial states for the iteration process, presented in Section 3, Fig. 2. Huang et al. [7] used the initial state denoted v1 in Fig. 2. However, in our study it was observed that v2 initial configuration led to the highest results for traction and shear conditions.

SPH-SQ can be considered the best design regarding tensile stiffness behaviour, because it presents the highest E/E_s values for the range of porosities under study. Other works in the literature have also highlighted high stiffness results using this design, such as in the work by Hollister and Lin [47] for the effective Young's modulus.

Some of the designs of this work have been analysed in the literature for some ranges of porosity. Here, we compare those values to the models developed in the present work. CCU was analysed by Cheng et al. [37] using experimental and numerical approaches, leading to similar results to those obtained in this work. Also the diagonal structure (DIAG) has been analysed in other works [17], and it was found that this design is not proper for tensile loading conditions. None of their trusses are oriented in the loading direction, which leads to low Young's modulus values. Octet truss (OCT) has been widely analysed in literature, although it was shown that it is one of the worst design for tensile conditions, with similar values to those obtained in literature [2,14]. It is worth noting that loading orientation can have a large influence on the behaviour of this design [14].

<u>Shear modulus G/G_s</u>

Shear modulus results for a variation of porosity between 10% and 90% are shown in Fig 9b. The numerical results are normalized by the nominal shear modulus corresponding to the nominal properties implemented in the model without porosity, following the equation $G_s = E_s/2(1+\nu)$, valid for solid homogenous isotropic materials. The trends obtained for G/G_s are different to those previously found for relative Young's modulus calculation. In general, results show less dispersion than for Young's modulus. A non-linear influence of porosity is observed for all the structures analysed, see Fig. 9b. The SPH-HEX configuration shows the best behaviour under shear conditions for porosities ranging between 10% and 60%. However, its shear stiffness properties decrease for higher porosities and other structures, such as DIAG, CCU-DIAG and OCT, present higher G/G_s values.

DIAG design also gives good results in terms of G/G_s values, while in tensile loading shows one of the worst behaviours. The diagonal distribution of the material for these configurations, with bars oriented at ±45° degrees, improves the behaviour under shear loading. The spheres distribution includes diagonal trusses of material in SPH-HEX case, leading to a similar effective configuration. In addition, the absence of stress concentrators in SPH-HEX leads to a better shear behaviour than that exhibited by the DIAG design for porosities up to 60%.

The random design TRUSS-RND shows the lowest shear performance for most of the porosities analysed and would be the lower bound of shear properties for the structures under study. This points out that randomness is undesirable to optimize a certain mechanical parameter. Concerning the effect of the randomness distribution, it is mainly observed in the in the SPH-RND distribution.

On the other hand, the results of several models fall in a narrow range of variation, see results of CCU-DIAG, SPH-SQ, OCT and OPT-E-TENS in Fig. 9b. Therefore, in terms of relative shear modulus (G/G_s) some of the morphometries lead to very similar results, with analogous behaviour for a variation of the model porosity.

Shear loading has been analysed in [7], however the initial state for the optimization was different (v1) than in this work (v2), which leads to slight differences in the final structure that can have an influence on the mechanical behaviour. This type of optimization was also studied for shear loading in [38], solving a 2D problem to create a micro-cellular structure, being a different problem providing no comparable results.

Poisson's ratio ν/ν_s

Fig. 10 shows the normalized Poisson's ratio (ν/ν_s) related to the value used for the bulk material in the numerical model for the cases analysed. As expected, values obtained for the models of low porosities are close to material Poisson's ratio. To the author's knowledge, Poisson's ratio has been poorly analysed in reticular and porous structures despite its importance in the compressibility of the structure.

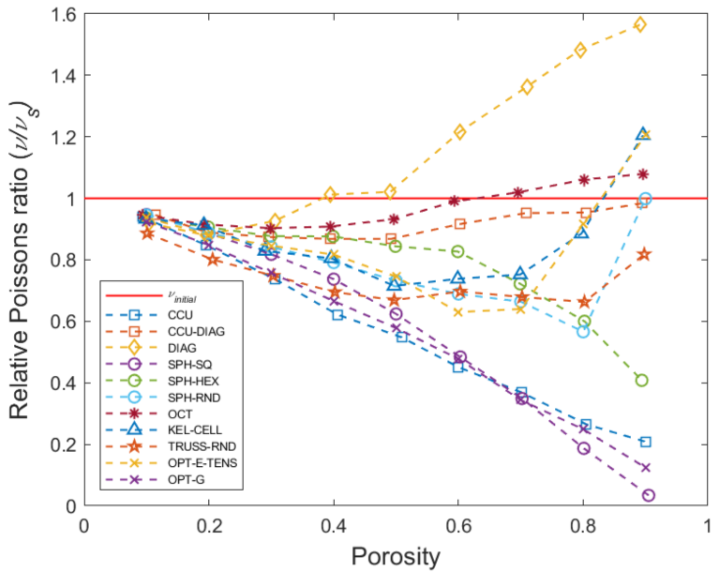

Figure 10. Results obtained for Poisson's ratio for models of different porosities. In this figure, the Poisson's ratios calculated using PBC have been divided by the material Poisson's ratio implemented in the numerical model.

When porosity increases, the Poisson's ratio experiences a strong dispersion depending on the configuration. Architectures with high Poisson's ratio present higher strains in the transverse direction when the load is applied in the longitudinal direction. Obviously, this is result from the morphometry and the subsequent deformation mechanisms of each structure. In DIAG configuration, Poisson's ratio reaches values close to ν=0.5, with porosity equal to 0.9. CCU-DIAG and OCT configurations present little variation on the relative Poisson's ratio with values nearby 1 for the porosities analysed. Both configurations have morphological similarities, like the diagonal bars of the RVE. In case SPH-HEX, Poisson's ratio is relatively constant up to a 60% of porosity, with values around 0.25. However, for larger porosities, Poisson's ratio decreases proportionally up to 0.12. The random configurations, SPH-RND and TRUSS-RND, are influenced similarly by the porosity level and the relative Poisson's ratio (ν/ν_s) takes decreasing values around 0.75. Strong variations can be found for large porosities in SPH-RND, due to its complex geometry.

On the other hand, some configurations show a Poisson's ratio decrease when porosity is close to 1, for instance CCU, OPT-G and SPH-SQ. Specifically, SPH-SQ presents a value about ν=0.01 for a 90% model porosity, close to auxetic materials, leading to low strains in transverse direction. For these three configurations, material is principally distributed at the RVE edges.

It is worth noting the variable trend of the Poisson's ratio for a change on porosity for the KEL-CELL and OPT-E-TENS configurations varying from low to high values. It is observed the influence of porosity on transverse strains, leading to higher compressive strains in the transverse direction to the load.

5.4. Stress-strain tension curves and fracture paths

Fig. 11 shows the stress-strain curves obtained in the tensile fracture simulation for each configuration. Experimentally, fracture tests on lattice structures are usually carried out under compressive loads, and only few works in the literature study the fracture process under tensile loading [48,49].

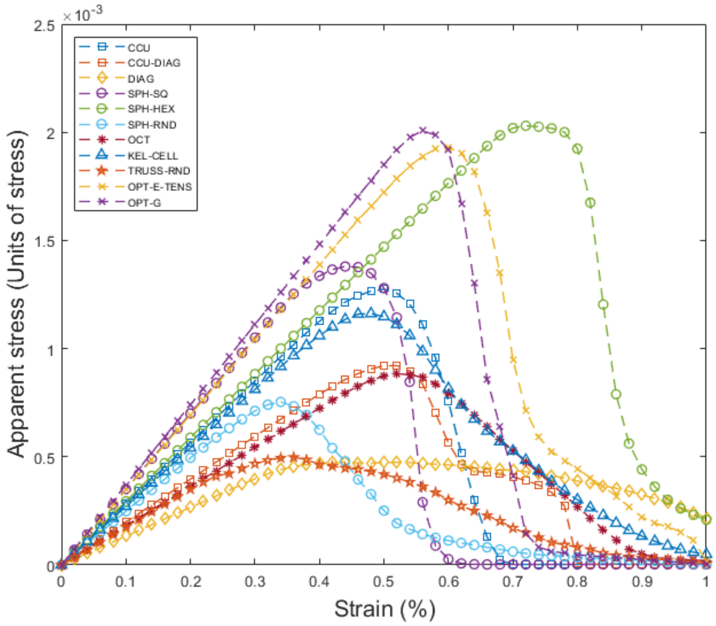

Figure 11. Stress-strain curves obtained for each design with porosities equal to 50% under tensile loading conditions until fracture.

Regarding the stiffness of the structure, results shown in Fig. 11 are similar to those shown in previous section, although small differences exist due to the non-periodic boundary conditions imposed in this simulation. Configurations presenting the highest stiffnesses are OPT-E-TENS, SPH-SQ and OPT-G, matching the highest strength values. There are slight differences when the stiffness of the structure is analysed using PBC or conventional tensile test, although the tendency of the values keeps similar.

Compression analyses in reticular structures in scientific literature show different stress-strain curves presenting several local stress maxima with a quasi-continuum increase of the stress and high level of deformation, where material densification occurs [13,50]. However, Fig. 11 shows curves with a unique maximum stress for each configuration followed by a strong decrease of the stress, which is expected for tension loading conditions. The mechanical properties imposed to the model that assume a purely elastic material and a fragile fracture criterion influence the trends observed in the stress/strain curves. Although the structures are composed by several bars, failure tends to be localized in fracture bands rather than spread, see Fig. 13. Moreover, bars fracture simultaneously leading to a macroscopic fragile behaviour. This effect is in agreement with the observations by Xu et al. with 3D printed lattice structures with PLA [48], where a fragile fracture behaviour is reported. In our study, CCU-DIAG presents a small second peak after the initial crack, because the longitudinal bars break before than the diagonal ones (see Fig. 11, CCU-DIAG stress-strain curve). Random structures (TRUSS-RND and SPH-RND) are able to support higher strains, due to the random distribution leading to bar failure at different loads depending on their orientation with respect to the loading direction. This same fact affects to the DIAG configuration, since all of its bars are oriented differently with respect to the loading direction. This exacerbates the effect of bar orientation leading to a great admissible strain and low stress peak.

Fig. 12a shows a scatter plot of the failure stress as a function of the apparent stiffness for a 50% porosity. The highest the apparent modulus is the greater the stress at failure. Therefore, for a 50% porosity level, the material distribution conditions both the elastic and failure properties following a linear relationship, with a coefficient of correlation ρ=0.87. This kind of behaviour have been observed in other foamed structures, such as cancellous bone [46]. On the other hand, the failure strain does not correlate to the apparent modulus, since a coefficient of correlation ρ=0.42 was obtained, see Fig. 12b.

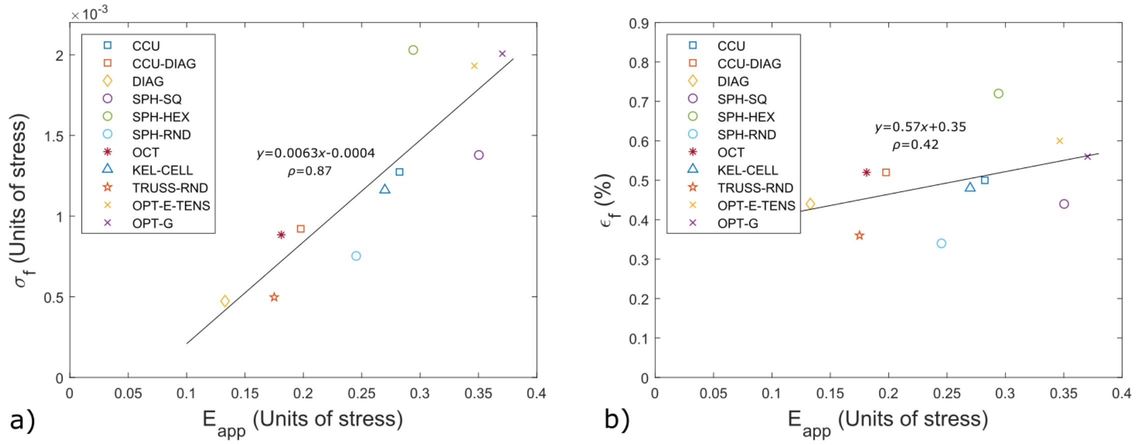

Figure 12. Scatter plot of a) failure stress and b) failure strain as a function of the apparent modulus of each structure.

Fracture paths obtained under tensile loading are shown in Fig. 13 for configurations with a porosity of 50%. Structures with connected bars show fracture paths located at bars joints due to the elevated stress concentration at these zones. Probably, the incorporation of fillets at these corners would improve the response of these structures to high stresses, increasing their maximum admissible load. Structures cut by spheres (SPH-SQ and SPH-HEX) present fracture paths in zones with small thickness walls due to the presence of voids. SPH-SQ is fractured by transverse fracture paths, while SPH-HEX also presents a diffuse fracture path at 45º with respect to the loading direction. These are maximum shear planes appearing in the structure due to the hexagonal distribution of the cutting spheres. Random structures mainly present two transverse fracture paths close to the upper and lower face. These fracture paths are more diffuse than those shown, for instance, in SPH-SQ due to the random distribution. Optimized structures also present transverse fracture paths located at the thinnest walls. Also OPT-E-TENS presents damaged areas close to the faces where boundary conditions were applied.

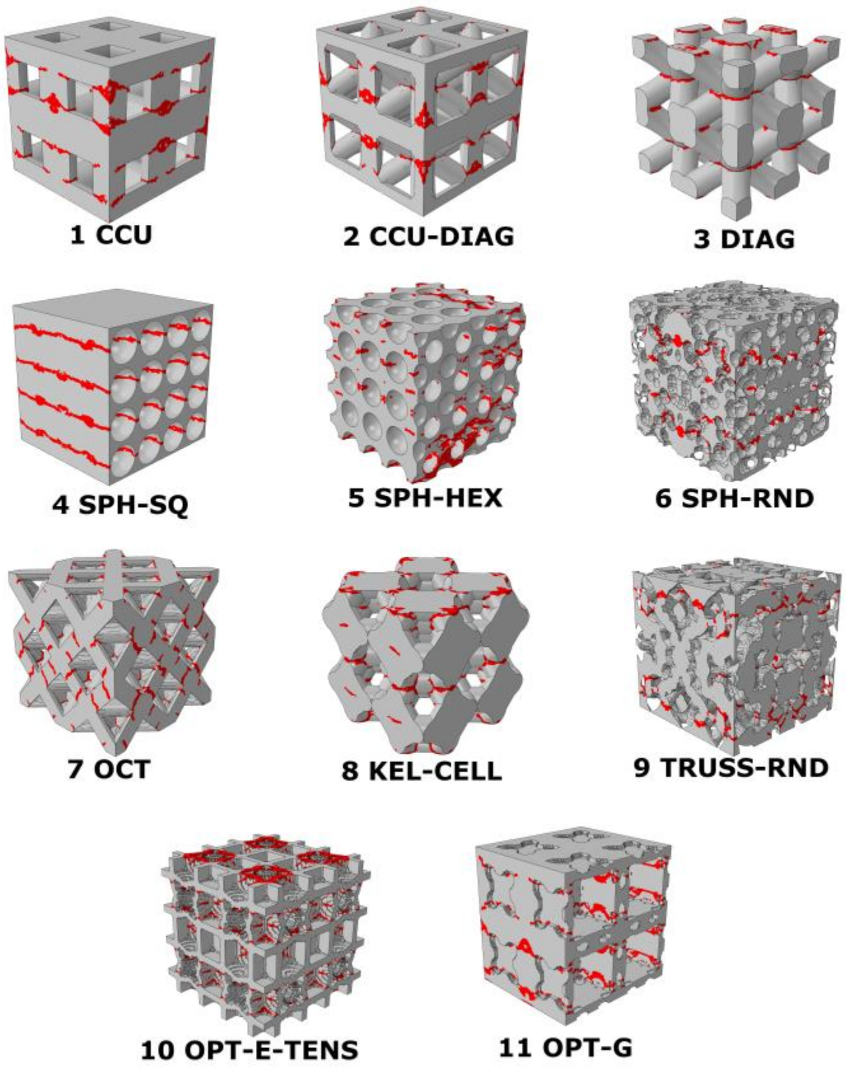

Figure 13. Simulation of fracture paths under tensile loading. The displacement is applied in vertical direction. Elements in red represent damaged elements while grey elements in grey intact material. SPH-SQ, SPH-HEX and OPT-G are cut through a plane to show an internal view. Porosity for all structures is 50%.

As explained above, fracture paths shown in this work are mainly transverse to the loading direction, except for SPH-HEX, where the hollow hexagonal distribution leads to some diagonal fracture planes, corresponding to maximum shear planes at 45º. This location of the fracture paths seems to be clearly influenced by the geometry of the structure. Some examples extracted from literature are shown in Fig. 14. Tensile fracture tests reported in the literature [48,49] show that an increased quantity of bars oriented with the same direction of load, leads to enhanced transverse fracture paths. The absence of longitudinal bars originates cracks following the bars located closer to the longitudinal axis (see for instance Fig. 14a from [49]). Compression tests reported in literature also highlight the strong influence of the structure design on the fracture path. Depending on the architecture, transverse fracture paths [15] or diagonal cracks [17] can be found. For example, in Fig. 14a and 14c, failure tends to concentrate in shear bands, which correspond to the maximum shear planes direction. Another failure mode observed in this kind of structures is the local buckling of the struts [15]. The presence of longitudinal or transverse bars only implies a transverse fracture path (see fracture under compression in Fig. 14b from [15]), while the use of also diagonal bars leads to a diagonal crack path (see Fig. 14c from [17]). Also, a bad quality of the PLA printed can influence the fracture path, leading to a more diffuse crack [51].

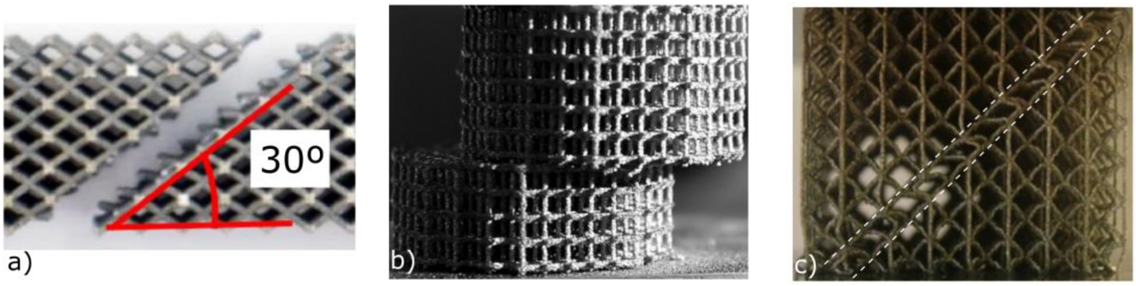

Figure 14. Some fracture paths reported in literature. a) Diagonal fracture path at 30º from [49]. b) Transverse fracture under compression due to local buckling from [15]. c) Diagonal fracture path at 45º under compression from [17]. Reprinted from Refs. [15,17,49] with permissions.

6. Conclusions

In this work, the mechanical behaviour of several lattice and porous structures has been modelled using finite element numerical models. This numerical analysis allowed the study of the mechanical behaviour of different configurations, obtained from the literature or developed through topological optimization. This kind of analysis is useful to understand the behaviour of each structure under different conditions, allowing the selection of a specific structure for a given loading case.

Numerical models have been validated comparing with experiments extracted from literature, leading to accurate results.

PBCs have been implemented aiming at estimating the stiffness matrix associated to each morphology and the subsequent mechanical properties for different levels of porosity. Regarding apparent Young’s modulus, the configurations with spherical cavities arranged in a square distribution yield the best results, because of the bulk material aligned with the loading direction. The topologic optimized configuration for this purpose also shows an enhanced behaviour, since it follows a similar distribution to that created by spherical cavities. The configuration with spherical cavities arranged in a hexagonal distribution leads to the best mechanical behaviour under shear loading. The increased distribution of material at the diagonal zone explains this behaviour. As expected, configurations with random distributions show a worse behaviour both in tensile and shear loading, due to the small effective area involved. As regards the Poisson's ratio, an interesting dispersion of the results has been found, showing strong variations as the porosity changes. This fact has led to either an increase or a decrease of the Poisson's ratio for high levels of porosity that depends on the structure.

Fracture has also been modelled for each structure to analyse the tensile stress-strain curve and the fracture path. Thus, the stiffness behaviour of the structures has been corroborated at the first loading stages. Random structures show that are not able to withstand high loads, since local damage initiates at the first steps of the loading process. However, the damage in these structures is more progressive, although its failure strain is similar to the ones for non-random structures. A linear relationship between the apparent stiffness and the stress at failure has been obtained. The highest the rigidity is, the greater the stress at failure. No significant correlation was found to the strain at failure. Fracture paths initiate principally at connections between bars that act as stress concentrators. In general, path propagation is clearly influenced by the material distribution in the structure.

In this work we have included the most important structures designed or studied in literature. Due to the large number of structures available in research, some of them have not been included in this work, which is a limitation of the paper. For instance, triply periodical minimal surface (TPMS) geometries such as gyroids have not been studied in this work, since the large number of design possibilities would make the paper difficult to follow and to understand.

Another limitation of the work is the fact that we only have analysed the ideal geometry of the structures by finite element models. However, these procedures can produce geometrical imperfections, such as porosity, variation in strut's thickness, residual stress and localised buckling due to bed's instabilities [34]. Also, the orientation of the 3D printing can influence its mechanical behaviour, leading to a structure with orthotropic behaviour, while here they have been considered as modelled by homogeneous materials. These imperfections could affect to the behaviour of the structure, reducing their mechanical properties like in this work have been analysed.

7. Acknowledgements

The authors gratefully acknowledge the funding support received from the Spanish Ministry of Economy and Competitiveness and the FEDER operation program for funding the projects DPI2017-89197-C2-1-R and DPI2017-89197-C2-2-R and the Generalitat Valenciana through the project Prometeo/2016/007.

8. References

[1] Wang Y, Zhang L, Daynes S, Zhang H, Feih S, Wang MY. Design of graded lattice structure with optimized mesostructures for additive manufacturing. Mater Des 2018;142:114–23. https://doi.org/10.1016/J.MATDES.2018.01.011.

[2] Deshpande VS, Fleck NA, Ashby MF. EEective properties of the octet-truss lattice material. J Mech Phys Solids 2001;49:1747–69.

[3] Gibson LJ, Ashby MF. Cellular solids : structure and properties. Cambridge University Press; 1999.

[4] RYAN G, PANDIT A, APATSIDIS D. Fabrication methods of porous metals for use in orthopaedic applications. Biomaterials 2006;27:2651–70. https://doi.org/10.1016/j.biomaterials.2005.12.002.

[5] Banhart J. Manufacture, characterisation and application of cellular metals and metal foams. Prog Mater Sci 2001;46:559–632. https://doi.org/10.1016/S0079-6425(00)00002-5.

[6] Hollister SJ. Porous scaffold design for tissue engineering. Nat Mater 2005;4:518–24. https://doi.org/10.1038/nmat1421.

[7] Huang X, Radman A, Xie YM. Topological design of microstructures of cellular materials for maximum bulk or shear modulus. Comput Mater Sci 2011;50:1861–70. https://doi.org/10.1016/j.commatsci.2011.01.030.

[8] Rafi HK, Karthik N V., Gong H, Starr TL, Stucker BE. Microstructures and mechanical properties of Ti6Al4V parts fabricated by selective laser melting and electron beam melting. J Mater Eng Perform 2013;22:3872–83. https://doi.org/10.1007/s11665-013-0658-0.

[9] Tkac J, Samborski S, Monkova K, Debski H. Analysis of mechanical properties of a lattice structure produced with the additive technology.

Compos Struct 2020;242. https://doi.org/10.1016/j.compstruct.2020.112138.

[10] Syam WP, Jianwei W, Zhao B, Maskery I, Elmadih W, Leach R. Design and analysis of strut-based lattice structures for vibration isolation. Precis Eng 2018;52:494–506. https://doi.org/10.1016/J.PRECISIONENG.2017.09.010.

[11] Montazerian H, Davoodi E, Asadi-Eydivand M, Kadkhodapour J, Solati-Hashjin M. Porous scaffold internal architecture design based on minimal surfaces: A compromise between permeability and elastic properties. Mater Des 2017;126:98–114. https://doi.org/10.1016/j.matdes.2017.04.009.

[12] Choy SY, Sun C-N, Leong KF, Wei J. Compressive properties of functionally graded lattice structures manufactured by selective laser melting. Mater Des 2017;131:112–20. https://doi.org/10.1016/J.MATDES.2017.06.006.

[13] Xiao Z, Yang Y, Xiao R, Bai Y, Song C, Wang D. Evaluation of topology-optimized lattice structures manufactured via selective laser melting. Mater Des 2018;143:27–37. https://doi.org/10.1016/j.matdes.2018.01.023.

[14] Messner MC. Optimal lattice-structured materials. J Mech Phys Solids 2016;96:162–83. https://doi.org/10.1016/J.JMPS.2016.07.010.

[15] Cuadrado A, Yánez A, Martel O, Deviaene S, Monopoli D. Influence of load orientation and of types of loads on the mechanical properties of porous Ti6Al4V biomaterials. Mater Des 2017;135:309–18. https://doi.org/10.1016/J.MATDES.2017.09.045.

[16] Ying J, Lu L, Tian L, Yan X, Chen B. ARTICLE IN PRESS Anisotropic porous structure modeling for 3D printed objects. Comput Graph 2017;7:1–8. https://doi.org/10.1016/j.cag.2017.07.008.

[17] McKown S, Shen Y, Brookes WK, Sutcliffe CJ, Cantwell WJ, Langdon GS, et al. The quasi-static and blast loading response of lattice structures. Int J Impact Eng 2008;35:795–810. https://doi.org/10.1016/J.IJIMPENG.2007.10.005.

[18] Gibson LJ, Ashby MF, Schajer GS, Robertson CI. The mechanics of two-dimensional cellular materials. Proc R Soc A Math Phys Eng Sci 1982;382:25–42.

[19] Gibson LJ, Ashby MF. The mechanics of three-dimensional cellular materials. Proc R Soc A Math Phys Eng Sci 1982;382:43–59.

[20] Marsavina L, Constantinescu DM, Linul E, Voiconi T, Apostol DA.

Shear and mode II fracture of PUR foams. Eng Fail Anal 2015;58:465–76. https://doi.org/10.1016/j.engfailanal.2015.05.021.

[21] Johnson AE, Keller TS. Mechanical properties of open-cell foam synthetic thoracic vertebrae. J Mater Sci Mater Med 2008;19:1317–23. https://doi.org/10.1007/s10856-007-3158-7.

[22] Fürst D, Senck S, Hollensteiner M, Esterer B, Augat P, Eckstein F, et al. Characterization of synthetic foam structures used to manufacture artificial vertebral trabecular bone. Mater Sci Eng C 2017;76:1103–11. https://doi.org/10.1016/j.msec.2017.03.158.

[23] Ashby MF. Metal foams : a design guide. Butterworth-Heinemann; 2000.

[24] Nie Z, Lin Y, Tong Q. Modeling structures of open cell foams. Comput Mater Sci 2017;131:160–9. https://doi.org/10.1016/j.commatsci.2017.01.029.

[25] Li D, Liao W, Dai N, Xie YM. Anisotropic design and optimization of conformal gradient lattice structures. CAD Comput Aided Des 2020;119:1–15. https://doi.org/10.1016/j.cad.2019.102787.

[26] Bendsøe MP, Kikuchi N. Generating optimal topologies in structural design using a homogeneization method. Comput Methods Appl Mech Eng 1988;71:197–224.

[27] Bendsøe MP. Optimal shape design as a material distribution problem. Struct Optim 1989;1:193–202. https://doi.org/10.1007/BF01650949.

[28] Wang MY, Wang X, Guo D. A level set method for structural topology optimization. Comput Methods Appl Mech Engrg 2003;192:227–46.

[29] Xie YM, Steven GP. ESO for Shape Optimization and the Reduction of Stress Concentrations. Evol. Struct. Optim., London: Springer London; 1997, p. 126–47. https://doi.org/10.1007/978-1-4471-0985-3_8.

[30] Xie YM, Steven GP. A simple evolutionary procedure for structural optimization. Comput Struct 1993;49:885–96. https://doi.org/10.1016/0045-7949(93)90035-C.

[31] Querin OM, Steven GP, Xie YM. Evolutionary structural optimisation (ESO) using a bidirectional algorithm. Eng Comput 1998;15:1031–48. https://doi.org/10.1108/02644409810244129.

[32] Huang X, Xie YM. Convergent and mesh-independent solutions for the bi-directional evolutionary structural optimization method. Finite Elem Anal Des 2007;43:1039–49.

https://doi.org/10.1016/J.FINEL.2007.06.006.

[33] Wang X, Xu S, Zhou S, Xu W, Leary M, Choong P, et al. Topological design and additive manufacturing of porous metals for bone scaffolds and orthopaedic implants: A review. Biomaterials 2016;83:127–41. https://doi.org/10.1016/j.biomaterials.2016.01.012.

[34] Peng C, Tran P, Nguyen-Xuan H, Ferreira AJM. Mechanical performance and fatigue life prediction of lattice structures: Parametric computational approach. Compos Struct 2020;235. https://doi.org/10.1016/j.compstruct.2019.111821.

[35] Zuo ZH, Xie YM. A simple and compact Python code for complex 3D topology optimization. Adv Eng Softw 2015;85:1–11. https://doi.org/10.1016/j.advengsoft.2015.02.006.

[36] Duan S, Xi L, Wen W, Fang D. Mechanical performance of topology-optimized 3D lattice materials manufactured via selective laser sintering. Compos Struct 2020;238. https://doi.org/10.1016/j.compstruct.2020.111985.

[37] Methods C, Mech A, Cheng L, Bai J, To AC. ScienceDirect Functionally graded lattice structure topology optimization for the design of additive manufactured components with stress constraints. Comput Methods Appl Mech Eng 2019;344:334–59. https://doi.org/10.1016/j.cma.2018.10.010.

[38] Du Y, Li H, Luo Z, Tian Q. Topological design optimization of lattice structures to maximize shear stiffness. Adv Eng Softw 2017;112:211–21. https://doi.org/10.1016/J.ADVENGSOFT.2017.04.011.

[39] Vercher A, Giner E, Arango C, Tarancón JE, Fuenmayor FJ, Vercher A, et al. Homogenized stiffness matrices for mineralized collagen fibrils and lamellar bone using unit cell finite element models. Biomech Model Mechanobiol 2014;13:437–49. https://doi.org/10.1007/s10237-013-0507-y.

[40] Reisinger AG, Pahr DH, Zysset PK. Elastic anisotropy of bone lamellae as a function of fibril orientation pattern. Biomech Model Mechanobiol 2011;10:67–77. https://doi.org/10.1007/s10237-010-0218-6.

[41] Hohe J. A direct homogenization approach for determination of the stiffness matrix for microheterogeneous plates with application to sandwich panels. Compos Part B 2003;34:615–626.

[42] ABAQUS/Standard User's Manual, v. 6.12. Providence, Rhode Island: Simulia; 2012.

[43] Giner E, Belda R, Arango C, Vercher-Martínez A, Tarancón JE, Fuenmayor FJ. Calculation of the critical energy release rate Gc of the cement line in cortical bone combining experimental tests and finite element models. Eng Fract Mech 2017;184:168–82. https://doi.org/10.1016/J.ENGFRACMECH.2017.08.026.

[44] Marco M, Giner E, Larraínzar-Garijo R, Caeiro JR, Miguélez MH. Modelling of femur fracture using finite element procedures. Eng Fract Mech 2018;196:157–67. https://doi.org/10.1016/j.engfracmech.2018.04.024.

[45] Marco M, Giner E, Caeiro-Rey JR, Miguélez MH, Larraínzar-Garijo R. Numerical modelling of hip fracture patterns in human femur. Comput Methods Programs Biomed 2019;173:67–75. https://doi.org/10.1016/J.CMPB.2019.03.010.

[46] Belda R, Palomar M, Peris-Serra JL, Vercher-Martínez A, Giner E. Compression failure characterization of cancellous bone combining experimental testing, digital image correlation and finite element modeling. Int J Mech Sci 2020;165:105213. https://doi.org/10.1016/j.ijmecsci.2019.105213.

[47] Hollister SJ, Lin CY. Computational design of tissue engineering scaffolds. Comput Methods Appl Mech Eng 2007;196:2991–8. https://doi.org/10.1016/J.CMA.2006.09.023.

[48] Xu Y, Zhang H, Šavija B, Chaves Figueiredo S, Schlangen E. Deformation and fracture of 3D printed disordered lattice materials: Experiments and modeling. Mater Des 2019;162:143–53. https://doi.org/10.1016/J.MATDES.2018.11.047.

[49] Geng X, Lu Y, Liu C, Li W, Yue Z. Fracture characteristic analysis of cellular lattice structures under tensile load. Int J Solids Struct 2019;163:170–7. https://doi.org/10.1016/J.IJSOLSTR.2019.01.006.

[50] Yan C, Hao L, Hussein A, Raymont D. Evaluations of cellular lattice structures manufactured using selective laser melting. Int J Mach Tools Manuf 2012;62:32–8. https://doi.org/10.1016/J.IJMACHTOOLS.2012.06.002.

[51] Dong G, Wijaya G, Tang Y, Zhao YF. Optimizing process parameters of fused deposition modeling by Taguchi method for the fabrication of lattice structures. Addit Manuf 2018;19:62–72. https://doi.org/10.1016/J.ADDMA.2017.11.004.

Appendix A

Table I. Relative mechanical constants for different porosities. CCU structure

	0.1	0.2	0.3	0.4	0.5	0.6	0.7	0.8	0.9
E_{rel}	0.820	0.637	0.480	0.389	0.280	0.219	0.144	0.092	0.037
G_{rel}	0.807	0.583	0.388	0.247	0.149	0.080	0.040	0.010	0.004
ν_{rel}	0.940	0.848	0.737	0.622	0.548	0.451	0.369	0.265	0.208

Table II. Relative mechanical constants for different porosities. CCU-DIAG structure

	0.1	0.2	0.3	0.4	0.5	0.6	0.7	0.8	0.9
E_{rel}	0,745	0,592	0,414	0,289	0,220	0,130	0,078	0,056	0,023
G_{rel}	0,779	0,623	0,467	0,336	0,248	0,160	0,100	0,069	0,030
ν_{rel}	0,946	0,889	0,874	0,868	0,868	0,916	0,952	0,954	0,984

Table III. Relative mechanical constants for different porosities. DIAG structure

	0.1	0.2	0.3	0.4	0.5	0.6	0.7	0.8	0.9
E_{rel}	0,760	0,588	0,378	0,240	0,184	0,080	0,033	0,013	0,003
G_{rel}	0,771	0,619	0,471	0,368	0,290	0,200	0,131	0,084	0,039
ν_{rel}	0,919	0,880	0,927	1,012	1,021	1,216	1,363	1,483	1,565

Table IV. Relative mechanical constants for different porosities. SPH-SQ structure

	0.1	0.2	0.3	0.4	0.5	0.6	0.7	0.8	0.9
E_{rel}	0,839	0,710	0,596	0,488	0,377	0,269	0,200	0,139	0,059
G_{rel}	0,812	0,639	0,487	0,353	0,233	0,138	0,074	0,028	0,005
ν_{rel}	0,947	0,886	0,818	0,737	0,624	0,484	0,349	0,187	0,034

Table V. Relative mechanical constants for different porosities. SPH-HEX structure

	0.1	0.2	0.3	0.4	0.5	0.6	0.7	0.8	0.9
E_{rel}	0,880	0,713	0,581	0,444	0,353	0,257	0,171	0,100	0,066
G_{rel}	0,836	0,686	0,552	0,431	0,315	0,211	0,110	0,044	0,007
ν_{rel}	0,936	0,906	0,877	0,876	0,844	0,827	0,722	0,600	0,408

Table VI. Relative mechanical constants for different porosities. SPH-RND structure

	0.1	0.2	0.3	0.4	0.5	0.6	0.7	0.8	0.9
E_{rel}	0,817	0,647	0,482	0,476	0,256	0,254	0,092	0,031	0,006
G_{rel}	0,804	0,611	0,449	0,425	0,218	0,198	0,062	0,019	0,002
ν_{rel}	0,946	0,887	0,842	0,791	0,732	0,689	0,664	0,566	0,999

Table VII. Relative mechanical constants for different porosities. OCT structure

	0.1	0.2	0.3	0.4	0.5	0.6	0.7	0.8	0.9
E_{rel}	0,804	0,582	0,398	0,274	0,182	0,114	0,075	0,035	0,016
G_{rel}	0,816	0,645	0,479	0,350	0,247	0,171	0,116	0,058	0,027
ν_{rel}	0,946	0,915	0,903	0,908	0,932	0,990	1,019	1,061	1,079

Table VIII. Relative mechanical constants for different porosities. KEL-CELL structure

	0.1	0.2	0.3	0.4	0.5	0.6	0.7	0.8	0.9
E_{rel}	0,853	0,649	0,546	0,381	0,304	0,191	0,125	0,061	0,013
G_{rel}	0,817	0,661	0,499	0,352	0,229	0,143	0,074	0,031	0,010
ν_{rel}	0,933	0,913	0,829	0,805	0,715	0,738	0,752	0,885	1,205

Table IX. Relative mechanical constants for different porosities. TRUSS-RND structure

	0.1	0.2	0.3	0.4	0.5	0.6	0.7	0.8	0.9
E_{rel}	0,707	0,514	0,375	0,283	0,179	0,112	0,068	0,033	0,009
G_{rel}	0,711	0,498	0,345	0,234	0,153	0,085	0,050	0,022	0,005
ν_{rel}	0,886	0,801	0,748	0,695	0,669	0,697	0,679	0,663	0,818

Table X. Relative mechanical constants for different porosities. OPT-E-TENS structure

	0.1	0.2	0.3	0.4	0.5	0.6	0.7	0.8	0.9
E_{rel}	0,830	0,691	0,560	0,441	0,343	0,301	0,198	0,068	0,012
G_{rel}	0,791	0,627	0,490	0,371	0,249	0,179	0,119	0,058	0,005
ν_{rel}	0,937	0,880	0,846	0,817	0,745	0,630	0,640	0,916	1,206

Table XI. Relative mechanical constants for different porosities. OPT-G-TENS structure

	0.1	0.2	0.3	0.4	0.5	0.6	0.7	0.8	0.9
E_{rel}	0,843	0,707	0,581	0,470	0,369	0,269	0,121	0,071	0,019
G_{rel}	0,777	0,590	0,440	0,334	0,240	0,167	0,022	0,006	0,0002
ν_{rel}	0,923	0,848	0,757	0,666	0,578	0,478	0,344	0,249	0,124